UC Office of the President
Recent Work

Title

Dynamic deformability of individual PbSe nanocrystals during superlattice phase transitions

Permalink

Journal

ISSN

Authors

Wang, Yu
Peng, Xinxing
Abelson, Alex
et al.

Publication Date

DOI

Peer reviewed

MATERIALS SCIENCE

Dynamic deformability of individual PbSe nanocrystals during superlattice phase transitions

Yu Wang[1,2]*, Xinxing Peng[1,3]*, Alex Abelson[4], Penghao Xiao[1], Caroline Qian[4], Lei Yu[1,2], Colin Ophus[5], Peter Ercius[5], Lin-Wang Wang[1], Matt Law[4], Haimei Zheng[1,2]†

The behavior of individual nanocrystals during superlattice phase transitions can profoundly affect the structural perfection and electronic properties of the resulting superlattices. However, details of nanocrystal morphological changes during superlattice phase transitions are largely unknown due to the lack of direct observation. Here, we report the dynamic deformability of PbSe semiconductor nanocrystals during superlattice phase transitions that are driven by ligand displacement. Real-time high-resolution imaging with liquid-phase transmission electron microscopy reveals that following ligand removal, the individual PbSe nanocrystals experience drastic directional shape deformation when the spacing between nanocrystals reaches 2 to 4 nm. The deformation can be completely recovered when two nanocrystals move apart or it can be retained when they attach. The large deformation, which is responsible for the structural defects in the epitaxially fused nanocrystal superlattice, may arise from internanocrystal dipole–dipole interactions.

INTRODUCTION

Nanocrystals are often more susceptible to morphological changes than their bulk counterparts (1, 2), leading to unique physical and chemical properties (3–5). For instance, semiconductor nanocrystals form connected two-dimensional (2D) or 3D networks with necking between the neighboring nanocrystals (6, 7), which may result in Dirac cones and high charge carrier mobility (8, 9). Although there have been intensive studies on nanocrystal superlattices (10–15), how individual nanocrystal changes shape during superlattice transformations is generally unknown (16, 17). An understanding of how individual nanocrystal shape distortions contribute to the structural disorder of superlattices and thus the emergence of novel properties is significant. This knowledge is crucial not only for designing nanocrystals and nanocrystal architectures with the desired properties for various applications but also for controlling the physical and chemical processes of a wide range of matter at the atomic or nanometer scale.

In situ x-ray scattering has been used to study nanocrystal superlattice phase transitions by tracing the evolution of nanocrystal orientation, internanocrystal distance, and superlattice symmetry (16–18). However, it is a great challenge to obtain structural and morphological information of individual nanocrystals, especially considering the heterogeneous deformation behavior in an ensemble of nanocrystals. In situ liquid-phase transmission electron microscopy (TEM) is a powerful tool for studying individual nanocrystals with high resolution during dynamic processes such as nucleation (19, 20), growth (21–25), and etching (26, 27). However, investigating the nanocrystal superlattice formation and phase transitions generally requires the evaporation of solvents and the displacement of surface ligands (17), which is beyond the existing in situ liquid-phase TEM capabilities.

Here, we report real-time imaging of individual PbSe nanocrystals during superlattice phase transitions by our development of a facile liquid-phase TEM technique. We find that upon ligand removal, nanocrystals change shape drastically when approaching one another within a distance of 2 to 4 nm. The large deformation is fully recoverable. By combining high-resolution in situ movies with a 3D atomistic reconstruction of the highly monodisperse nanocrystals from ex situ scanning TEM (STEM) imaging, we quantify the deformation of nanocrystals during ligand displacements through different chemical treatments. We evaluate the deformation mechanisms with the aid of molecular dynamic (MD) simulations.

RESULTS AND DISCUSSION

Experimental setup of in situ liquid-phase TEM

We achieve the superlattice phase transitions with an effective "carbon film liquid cell," as shown in Fig. 1A. This method allows us to start with the hexagonal superlattice of oleate-capped nanocrystals instead of the colloid solution of nanocrystal monomers, thus avoiding the intractable solution evaporation inside the liquid cell during in situ TEM (detailed in fig. S1). We first treated two ultrathin (10 nm) TEM carbon grids with oxygen/argon plasma for 30 s to produce hydrophilic surfaces for improved wetting of the highly polar ethylene glycol (EG) solution. An unconnected hexagonal PbSe superlattice is formed on one of the treated carbon grids by evaporating 4 μl of hexane solution (0.5 mg/ml) of 6.2-nm PbSe nanocrystals capped with oleate ligands (fig. S2A). Then, 100 nl of a 15 mM solution of 1,2-ethylenediamine (EDA) in EG is deposited on the other carbon grid. The two carbon grids are then sandwiched into a TEM holder to form a carbon film liquid cell in which the nanocrystals undergo superlattice phase transitions due to gradual removal of the oleate ligand species by complexation with EDA.

Superlattice phase transition of PbSe nanocrystals in EDA solution

Figure 1B and movie S1 show a representative oriented attachment of six PbSe nanocrystals during the phase transition from a 2D hexagonal monolayer to a 1D chain. During this process, the translational and rotational movements and the shape changes of individual nanocrystals occur concurrently within approximately the first 10 s. We find that

[1]Materials Sciences Division, Lawrence Berkeley National Laboratory, Berkeley, CA 94720, USA. [2]Department of Materials Science and Engineering, University of California, Berkeley, Berkeley, CA 94720, USA. [3]State Key Lab of Physical Chemistry of Solid Surfaces, Collaborative Innovation Center of Chemistry for Energy Materials, College of Chemistry and Chemical Engineering, Xiamen University, Xiamen, 361005, P. R. China. [4]Department of Chemistry, University of California, Irvine, Irvine, CA, 92697, USA. [5]National Center for Electron Microscopy, Molecular Foundry, Lawrence Berkeley National Laboratory, Berkeley, CA 94720, USA.
*These authors contributed equally to this work.
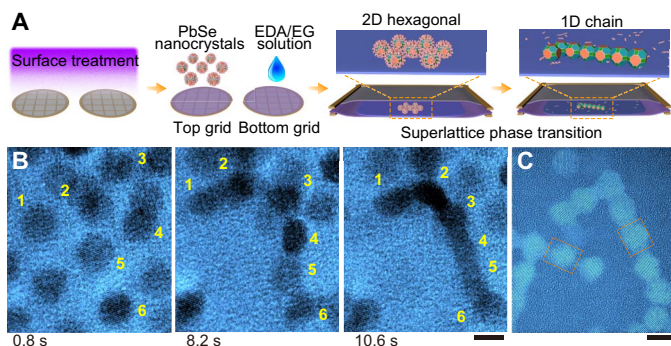†Corresponding author. Email: hmzheng@lbl.gov

Fig. 1. Experimental setup and superlattice phase transition of PbSe nanocrystals. (**A**) Schematic procedures for preparing a carbon grid liquid cell for in situ TEM. (**B**) Sequence of in situ TEM images showing the oriented attachment of six PbSe nanocrystals during the phase transition from 2D hexagonal monolayer to 1D nanocrystal chain. (**C**) High-resolution TEM image of the nanocrystal chains in vacuum. Orange rectangles indicate nanocrystals elongated along the internanocrystal axis. Scale bars, 5 nm.

nanocrystals dramatically change shape from truncated cuboctahedra elongated irregular ellipses when they approach each other within 2 to 4 nm (e.g., nanocrystals **3** and **4** in Fig. 1B). This deformation is directional, with elongation along the internanocrystal axis and shortening in the orthogonal directions. After recording the in situ movies, we dry the liquid and image the nanocrystal chains with aberration-corrected TEM (Fig. 1C). High-resolution images reveal the oriented attachment of {100} facets exclusively and confirm the elongation of certain nanocrystals in the chains as indicated by the rectangles in Fig. 1C.

Quantification of nanocrystal deformation through atomistic reconstruction

To quantify the nanocrystal shape changes, we compare the atomistic structure of the nanocrystals before and after oriented attachment using high-angle annular dark-field STEM (HAADF-STEM) imaging. We determine the 3D shape of an as-synthesized individual nanocrystal by analyzing high-resolution images of 32 nanocrystals oriented along various zone axes ([001], [110], [111], [211], and [310]). Representative images are shown in Fig. 2A and fig. S2 (B and C). Fast Fourier transform (FFT) analysis of the images demonstrates a rock salt PbSe crystal structure with a {200} lattice vector of 3.1 Å, same as that in bulk PbSe (28). We further count the number of Pb layers along the <111>, <100>, and <110> directions of each nanocrystal (Fig. 2B) and extract the distribution of the number of Pb layers along these three crystallographic directions (Fig. 2C). The nanocrystals have an average of 17.8, 20.0, and 29.8 Pb layers along the <111>, <100>, and <110> directions, respectively, with a standard deviation of less than one atomic layer. The resulting average 3D shape of the nanocrystals is shown in Fig. 2D and movie S2. Our statistical 3D reconstruction provides a more accurate nanocrystal morphology than what was previously available (16). It shows that the unfused nanocrystals are highly monodisperse, which simplifies the quantification of any shape changes during superlattice self-assembly and oriented attachment.

Oriented attachment of the nanocrystals in the presence of EDA resulted in the formation of nanocrystal chains. We define the length of each nanocrystal in a chain as the distance between the thinnest points of adjacent necks along the nanocrystal chain (vertical lines in Fig. 2E). Statistical analysis of 34 fused nanocrystals shows an average length and

width of 21.2 and 17.6 layers, respectively, revealing an approximately one-layer elongation along the internanocrystal axis and two-layer shrinkage along the orthogonal direction compared with the initial nanocrystal (Fig. 2F). In addition, the increased variances in the dimensions of the fused nanocrystals indicate that diverse shape changes occur during the superlattice phase transition. We note that nanocrystals in a chain prepared ex situ have the same dimensions as those formed in situ, proving that the observed shape changes are not an artifact of electron beam irradiation during TEM imaging.

Versatile deformation behavior of individual nanocrystals revealed by real-time imaging

We recorded high-resolution movies (movies S3 to S7) to reveal the versatile deformation behaviors of individual nanocrystals and details of the nanocrystal fusion process. Movie S3 and the image series in Fig. 3A depict the self-assembly and oriented attachment of three nanocrystals (**7**, **8**, and **9**). In the first image, the center-to-center distance between neighboring nanocrystals is 8.0 to 8.5 nm, and the gap distance is 2.0 to 2.5 nm (Fig. 3D). The nanocrystals then move toward each other and attach at ~3.0 s, as marked by the green arrow in Fig. 3D. The plot of center-to-center distances versus time shows that the approach speed is relatively slow from 0 to ~1.0 s and faster from ~1.0 to 3.0 s, suggesting the existence of attractive internanocrystal interaction during superlattice self-assembly (23). The nanocrystal **8** in the middle elongates from 6.5 to 7.2 nm while approaching the other two nanocrystals. During fusion, nanocrystals **7** and **8** show a matched {200} lattice aligned in the same direction with the same d-spacing of 3.1 Å, reflecting the nature of oriented attachment.

Unexpectedly, the elongation always reverses when nanocrystals subsequently move apart as observed in movies S3 to S6. Movie S4 and the image series in Fig. 3B depict a representative reversible shape change of a single nanocrystal. Nanocrystal **11** first elongates while approaching its neighbor (nanocrystal **12**) and then returns to a spherical shape after it moves farther away (>8 nm). Lattice fringes are visible throughout the movie, which allows us to confirm that the elongation is not a projection artifact caused by nanocrystal rotation. FFT analysis on each frame of movie S4 (Fig. 3C) shows no detectable change of the lattice spacing (3.1 Å), indicating that the elongation of nanocrystal results from an increased number of atomic planes along the <100> direction rather than lattice expansion. Figure 3E shows that the long axis elongates from 5.9 nm (19 layers counted along the <100> direction) at 0.2 s to 7.2 nm (23 layers) at 1.0 s and then fully recovers to 5.9 nm (19 layers) after 4.2 s, equivalent to a reversible elongation of 22%. Meanwhile, the width of the nanocrystal decreases from 5.9 nm at 0.2 s to 5.0 nm at 1.6 s and then recovers to 5.8 nm at 4.4 s (15% change). Accompanying the deformation of nanocrystal **11**, nanocrystal **12** also undergoes a reversible deformation, first stretching toward **11** and **13** and then recovering to a more spherical shape. We also measure the lattice fringes of nanocrystal **12** with a d-spacing of 3.1 Å, indicating that the deformation toward **13** is along the <100> direction as well, although the deformation toward **11** is unable to be determined precisely. Analyzing the center-to-center and gap distances of **11** and **12** (Fig. 3F), we find that the reversible deformation of nanocrystals occurs when they move apart from each other and the elongation toward each other makes the gap distance first decrease slightly in the first second and then increase because of the recovery from the elongated structures. The neighboring nanocrystals that move apart during the phase transition may arise from the separation of neighboring nanocrystals into two different nanocrystal chains, as detailed in fig. S3. Therefore, as
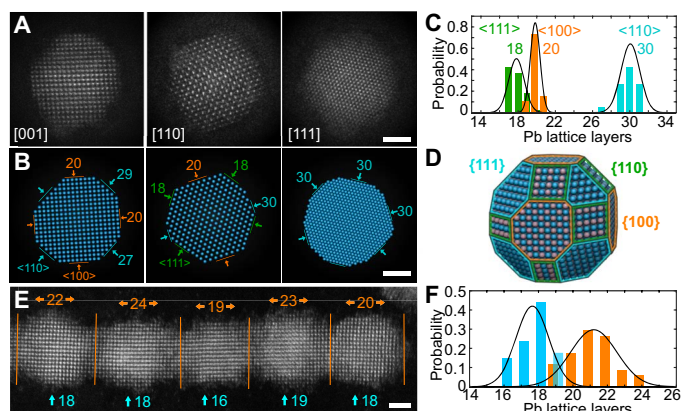
Fig. 2. Atomistic structure of the nanocrystals before and after oriented attachment. (**A**) HAADF-STEM images of three different nanocrystals before oriented attachment. Zone axes are labeled. (**B**) Corresponding atomic models of the three nanocrystals. Labels indicate the number of Pb layers along the <100> (orange), <110> (blue), and <111> (green) directions. (**C**) Histograms of the number of Pb layers along these three directions as obtained from analysis of 32 nanocrystals. (**D**) Reconstructed 3D model of the average nanocrystal before oriented attachment. Blue spheres, Pb; pink spheres, Se. Facets are labeled. (**E**) Representative HAADF-STEM image of a nanocrystal chain formed by oriented attachment. Vertical lines denote the nanocrystal boundaries, and labels indicate the number of Pb layers along the nanocrystal length (orange) and width (blue). (**F**) Histogram of nanocrystal length (orange) and width (blue) for 34 nanocrystals in several chains. Scale bars, 2 nm.

demonstrated above (Fig. 3, A to F) and summarized in Fig. 3G, the different translation modes of nanocrystals can lead to different deformation modes, i.e., the reversible deformation when moving apart and the retained deformation when moving toward a neighbor. The two deformation modes are also illustrated in movies S5 to S7 and figs. S4 and S5. The observed large deformability of PbSe semiconductor nanocrystals may arise from the intrinsic nanoscale property that the surface atoms of a nanocrystal are highly mobile during reconstruction (29, 30). In our experiment, the PbSe nanocrystals are exceedingly monodisperse. Systematic study is needed to elucidate the size effects on the deformability of PbSe semiconductor nanocrystals. We speculate that the deformability of PbSe nanocrystals decreases, as the size of the nanocrystal increases.

Reduced nanocrystal deformability in the absence of EDA

To investigate how the nanocrystal deformability responds to the solution environment, we have performed the superlattice phase transition in pure EG. With the absence of EDA, in situ movie S8 and Fig. 4 reveal a superlattice transformation from unconnected hexagonal to connected square. We found that the square superlattice forms about 10 times slower than the nanocrystal chains, which is as expected, since EDA removes oleate ligand species much faster than EG does (8, 31). In pure EG, the nanocrystals do not change shape before fusion. The measurement of four representative nanocrystals **14** to **17** (Fig. 4D) shows that the long axis–to–short axis ratio is less than 1.06 during the entire self-assembly process, in contrast to a ratio as high as 1.3 for nanocrystals in EDA solution. Reduced deformation of nanocrystals in EG is also shown in movie S9 and fig. S6. Note that the movies in EG and in EDA/EG were acquired using very similar electron current density; nevertheless, the nanocrystals during superlattice phase transition in EG were not deformed before fusion despite the larger accumulated electron dose.

The different deformation behavior in EG and EDA/EG strongly affects the formation processes and structural perfection of the superlattice. As shown in fig. S7, although similar square superlattices can be obtained in both EG and EDA/EG with a high concentration of nanocrystals, the pathways are different: topologically symmetric growth through small squares to large squares in EG and asymmetric growth through the merging of nanocrystal chains in EDA/EG. Since nanocrystals in pure EG maintain their original shape during self-assembly, the resulting superlattices are more uniform and less defective (e.g., fewer missing connections) (9, 12).

Proposed mechanisms of nanocrystal deformation

As shown above, in contrast to the conventional view, which considers the nanocrystal having a rigid shape during superlattice self-assembly before the nanocrystals connect with each other, we found that the nanocrystals can drastically change shape within a distance of 2 to 4 nm and they change shapes before touching each other. This shows that nanocrystals are not rigid once their surface ligands are removed. It also shows that there is a "long"-range interaction, which is not induced by ligands. One possibility for such long-range interaction is the electrostatic dipole–dipole interaction. Previous studies suggested that PbSe nanocrystals self-assemble into chains in EDA/EG as a result of electric dipole interactions between nanocrystals generated by the uneven removal of Pb oleate species on the {111} facets (10, 32, 33). Using energy-dispersive x-ray spectroscopy (EDS), we find that the atomic ratios of Pb and Se in hexagonal superlattices, square superlattices, and chains are 57:43, 51:49, and 50:50, respectively (fig. S8). This confirms the removal of excess Pb atoms along with the oleate ligands during superlattice transformations, which is consistent with the previous results from nuclear magnetic resonance and infrared spectroscopy (34). A schematic of EDA-induced ligand removal and the corresponding chemical structures are shown in fig. S9.

Molecular dynamic simulations

We performed MD simulations to testify our hypothesis of dipole–dipole interaction–induced deformation. Lennard-Jones (LJ) potential and Coulomb interactions are included in the classical force field Hamiltonian. Such a model Hamiltonian can be used to describe the rock salt structure of PbSe nanocrystals and the Pb cation and Se anion movement in the solvent (although no explicit solvent molecule is used) (30, 35). As shown in Fig. 5A, polar nanocrystals tend to become symmetrized through surface atom diffusion (30). Note that direct dipole moment calculation shows a strong dipole moment at 10 ps that is 25% of the original dipole moment at 0 ps. Nevertheless, the surface atom diffusion of polar nanocrystal monomer does not lead to formation of extra lattice fringes along <100> directions. In contrast, Fig. 5B shows that two polarized nanocrystals with 20 layers along their <100> directions are initially aligned in the same dipole direction with a gap distance of 2 nm. During the MD simulation, some of the surface atoms diffuse out to form an elongated shape along the dipole direction. This happens before the nanocrystals touch each other. After the two nanocrystals attach, the deformations of the nanocrystals are mostly retained, yielding an elongated dimer with 41 layers along the internanocrystal direction, resembling the schematic where nanocrystals move together in Fig. 3G. The dimer keeps its elongated 41-layer structure in longer simulations probably because the dipole in the systems has been reduced to a low and stable level (3% change from 50 to 233 ps). The shape stability of a nondipolar nanocrystal is also reflected in fig. S10, which shows that even at higher temperature (600 K), the shape changes
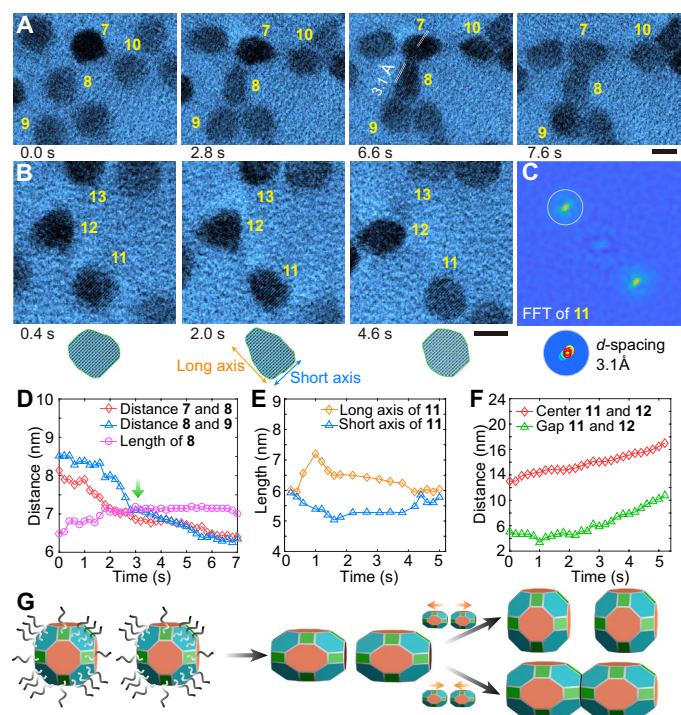
Fig. 3. Dynamic deformability of individual PbSe nanocrystals. (**A**) Sequence of in situ TEM images showing the elongation of nanocrystal **8** during the oriented attachment with nanocrystals **7** and **9**. White lines in the third image indicate the matched {200} lattices of two attaching nanocrystals with a *d*-spacing of 3.1 Å. (**B**) Sequence of TEM images and reconstructed models showing reversible deformation of nanocrystal **11** during moving apart from the neighbor nanocrystal **12**. (**C**) Superimposed FFT images of **11** in each movie frame during the reversible deformation. The zoomed-in region shows the overlap of the diffraction spot in each frame with a consistent {200} *d*-spacing of 3.1 Å. (**D**) Time-dependent changes of the length of **8** along the internanocrystal direction and the center-to-center distances between **7**, **8**, and **9**. Green arrow marks the time that three nanocrystals attached. (**E**) Reversible changes of the long and short axial length of **11**. (**F**) Time-dependent changes of center-to-center distance and gap distance between **11** and **12**. (**G**) Two deformation modes corresponding to two different motions, i.e., the reversible deformation when nanocrystals move apart and the retained deformation when they move toward and attach. Scale bars, 5 nm.

Fig. 4. Reduced deformation during the superlattice transformation in EG. (**A**) Sequence of in situ TEM images showing reduced deformation of nanocrystals during the phase transition from oleate-capped hexagonal to epitaxially fused square superlattice. (**B**) Large-area TEM image observed in situ showing the uniformity of nanocrystals in the square superlattice. (**C**) STEM image of a dried square superlattice showing the necks between nanocrystals. (**D**) Ratio of the long and short axes of four representative nanocrystals (**14** to **17**) changes much smaller in EG than that of nanocrystal **11** in EDA solution. Scale bar, 5 nm (A) and 20 nm (B and C).

of a nondipolar dimer are minimal. Alternatively, three aligned dipolar nanocrystals are simulated as shown in Fig. 5C with the centers of the two outside nanocrystals fixed, whereas the middle nanocrystal is free to move, imitating the situation of the boundary of two superlattice matrices. The outside nanocrystals belong to different matrices and cannot move toward the center to get attached with the middle one directly (fig. S3). At 9 and 50 ps, the MD shows a reversible elongation of the middle nanocrystal, which is similar to the experimental observation when two nanocrystals move apart in Fig. 3B. After that, the recovered middle nanocrystal keeps its 20-layer structure, gradually moves to the nanocrystal on the right, and attaches to it. Although these simulated deformations are less dramatic compared to the observed ones in Fig. 3, we have to be mindful for the limitation of the simple force field model, which might be too restrictive to allow the Pb^{2+} and Se^{2-} ions to diffuse out from the nanocrystals. Nevertheless, what we demonstrated here is the tendency of the dipole–dipole interaction leading to nanocrystal deformation before they touch each other. To further confirm that this tendency is caused by the dipole–dipole interaction, we have also simu-
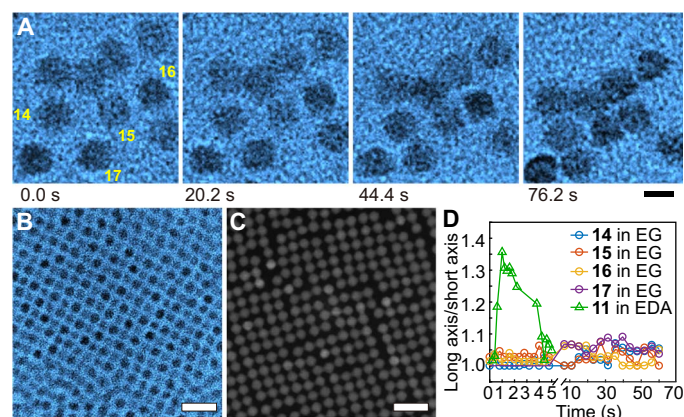
lated cases where no dipole moment exists at 0 ps. As shown in fig. S10, no elongation of nanocrystals is observed, even at a higher temperature.

It is worth mentioning that our current MD simulation is based on a very simple LJ plus electrostatic potential, which lacks the accurate description of the covalent bonding, surface energy, ligand passivation, as well as the solvent molecule effects. Hence, it can only provide a qualitative picture. It is mainly used to address the qualitative question: Whether the dipole–dipole interaction can provide the energetic driving force for the shape deformation. Since this model does have the electrostatic ion-ion interaction and it forms the rock salt crystal structure of PbSe in bulk form, we believe that it is capable of answering our qualitative questions. Nevertheless, to simulate the process more quantitatively, one has to include accurate surface energy, ion-ligand interaction, ion-solvent molecule interaction, as well as the accurate energy for covalent bond breaking and forming (*36, 37*). Right now, this classical potential is not readily available for the PbSe system. Some of the new developments for neural-network force field trained on the basis of ab initio data might provide hope for a more automatic procedure to develop these classical potentials in the future.

CONCLUSION
Our real-time observations reveal an unexpected phenomenon that PbSe semiconductor nanocrystals can drastically change shape during superlattice phase transitions. The deformability of semiconductor nanocrystals can be controlled by the chemical environments upon ligand removal, as illustrated in the PbSe nanocrystal system. EDA-induced oleate removal increases the nanocrystal dipole–dipole interactions, triggering the large shape changes and rapid nanocrystal fusion. After the ligands are removed, PbSe nanocrystals experience drastic directional shape deformation when the spacing between two nanocrystals reaches 2 to 4 nm. Moreover, the deformation can be completely recovered when two nanocrystals move apart or it can be retained when they attach. Controlling nanocrystal deformation during ligand removal or ligand exchange is critical to achieve the structural perfection of
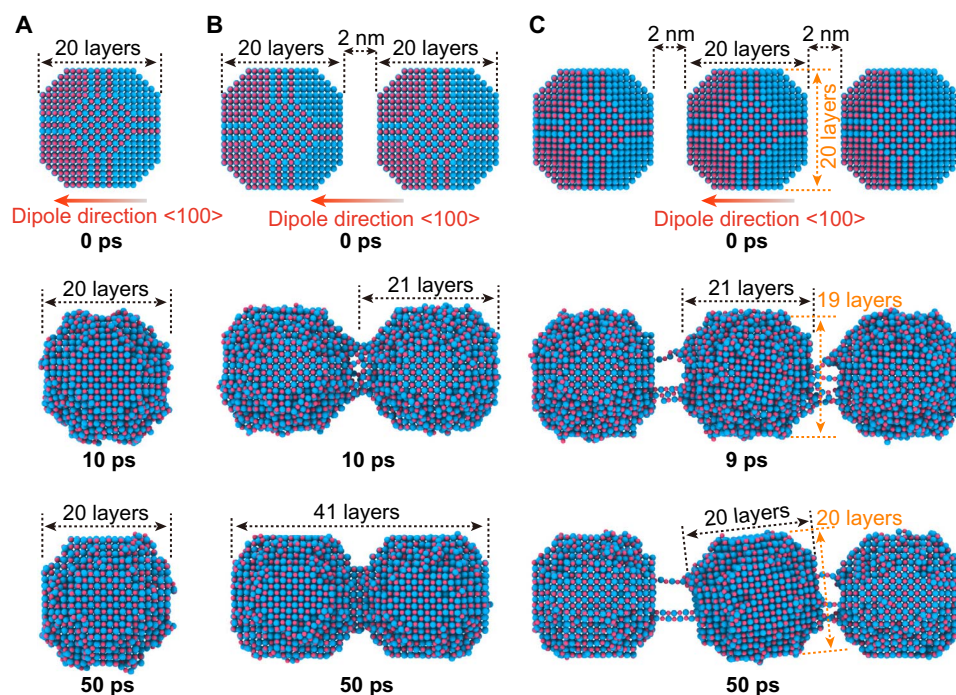
Fig. 5. Molecular dynamics simulation on the deformability of polar nanocrystals. Atom color code: blue, Pb; pink, Se. (**A**) Snapshots of the trajectory of single-dipolar nanocrystal at 300 K, starting with a dipole moment caused by fast ligand removal. Polar nanocrystal monomer exhibits the tendency to become symmetrized through surface atom diffusion; nevertheless, this does not lead to formation of extra lattice fringes along <100> directions. (**B**) Snapshots of the trajectory of two dipolar nanocrystals initially aligned along the dipole direction with a gap distance of 2 nm at 300 K. Translation and rotation of the two nanocrystals centers are not restricted, allowing them to move toward each other and get attached, thus to simulate the moving-toward motion in Fig. 3A. Although the two nanocrystals move toward each other, their deformation happens before they touch each other, and the resulting edge-to-edge distance is 12.3 nm (41 layers) larger than the distance shown by two nanocrystals rigidly touch with each other (12.0 nm, 40 layers). (**C**) Snapshots of the trajectory of three dipolar nanocrystals aligned with the same dipole direction with gap distances of 2 nm at 300 K. Translation and rotation of the two outside nanocrystal centers are eliminated, whereas the middle one is free to translate and rotate, imitating the situation of the boundary of two superlattice matrices. The reversible elongation phenomena for the center nanocrystal resembles that in Fig. 3B.

nanocrystal superlattices; therefore, it could lead to performance enhancements in many applications of semiconductor nanocrystals, such as photoelectric devices, catalysis, plasmonic, and bioimaging.

MATERIALS AND METHODS
Materials
All commercially available chemicals including oleic acid (OA; technical grade, 90%), lead (II) oxide (PbO; 99.9995%; Alfa Aesar), selenium shot (99.999%), trioctylphosphine (TOP; technical grade, >97%; Strem Chemicals Inc.), 1-octadecene (ODE; 90%; Sigma-Aldrich), diphenylphosphine (DPP; 98%; Sigma-Aldrich), hexane (anhydrous; ≥99%; Sigma-Aldrich), EG (anhydrous; 99.8%; Sigma-Aldrich), EDA (anhydrous; Sigma-Aldrich), and ethyl alcohol (anhydrous; 99.5%; Sigma-Aldrich) were used as received. Ultrathin carbon film (10 nm, 400 mesh)–supported copper grids were purchased from Electron Microscopy Sciences.

PbSe nanocrystal synthesis
PbSe nanocrystals were synthesized and purified in a standard air-free environment as previously reported (*38*). Briefly, 1.50 g of PbO, 5.0 g of OA, and 10.0 g of ODE were thoroughly degassed under a dynamic vacuum of ~50 mTorr at 110°C for 1.5 hours. The solution was then heated to 180° ± 3°C under flowing argon, at which time 9.5 ml of a 1 M solution of TOP-Se containing 0.20 ml of DPP was quickly injected to start the nucleation. After a growth of 105 ± 3 s, the reaction was

quenched by a liquid nitrogen bath, removed from the liquid nitrogen, allowed to warm to 35°C, and diluted with 10 ml of anhydrous hexane. The nanocrystal product was washed three times using ethanol/hexane in a nitrogen-filled glove box [oxygen content less than 10 parts per million (ppm)], dried completely, and stored as a powder in the glove box. STEM analysis reveals that the as-synthesized nanocrystals are highly monodisperse with a diameter of 6.2 nm as shown in Fig. 2, A to D.

Liquid cell fabrication and TEM characterizations
Two ultrathin carbon film (10 nm, 400 mesh)–supported copper grids were treated by 25% oxygen/argon plasma for 30 s on a Fischione 1020 plasma cleaner to give hydrophilic surfaces for improved wetting of the EG solution. The fabrication of liquid cells was carried out in a nitrogen-filled glove box (oxygen content less than 10 ppm). A hexagonal superlattice was first formed on one of the treated carbon grids by drop-casting 4 μl of hexane solution (0.5 mg/ml) of PbSe nanocrystals, followed by the evaporation of hexane under 1 bar of nitrogen atmosphere in the glove box for 3 min. Then, 100 nl of the ligand removal solution (either 15 mM solution of EDA in EG or neat EG) was deposited on the other carbon grid. The two carbon grids were then sandwiched together and installed in a TEM holder (all under nitrogen atmosphere) to form a carbon grid liquid cell. The holder was then quickly removed from the glove box and inserted into the TEM for in situ characterization. The mechanism to initiate superlattice transitions is detailed in fig. S1. The Thermo Fisher Scientific (formerly FEI) ThemIS image aberration–corrected TEM at the Molecular Foundry

(MF), Lawrence Berkeley National Laboratory (LBNL) and JEOL 2100 TEM at Materials Science Division, LBNL were used for in situ observations. The microscope, operating voltage, and electron beam intensity for each experiment are indicated in the corresponding movie captions.

Ex situ experiments of the superlattice phase transition were started from the hexagonal superlattices prepared by the same drop-casting method for forming in situ liquid cells. The hexagonal superlattices on a carbon grid were then immersed in 15 mM solution of EDA in EG or neat EG for 1 min to form the nanocrystal chains or the square superlattice, respectively. Ex situ HAADF-STEM characterization of PbSe nanocrystal superlattices before and after ligand displacement was performed using the probe aberration–corrected Thermo Fisher Scientific (formerly FEI) Titan 80-300 named TEAM I (MF, LBNL). High-resolution TEM imaging and EDS were performed on image aberration–corrected Thermo Fisher Scientific ThemIS (MF, LBNL).

MD simulations

The MD simulations were performed using the Large-Scale Atomic/ Molecular Massively Parallel Simulator (LAMMPS) software package (39). Interactions between atoms were described by a pair potential including a short-range LJ part and a long-range Coulomb part

$$U_{ij}(r_{ij}) = U_{Coulomb}(r_{ij}) + U_{LJ}(r_{ij})$$
$$= \frac{q_i q_j}{4\pi\varepsilon_0 r_{ij}} + 4\varepsilon_{ij}\left[\left(\frac{\sigma_{ij}}{r_{ij}}\right)^{12} - \left(\frac{\sigma_{ij}}{r_{ij}}\right)^6\right] \quad (1)$$

The partial charges of PbSe and four LJ coefficients were taken from literature (30): $q_{Pb} = 1.29\ e$, $q_{Se} = -1.29\ e$, $\sigma_{Pb} = 3.29$ Å, $\sigma_{Se} = 4.36$ Å, $\varepsilon_{Pb}/k_B = 30.0$ K, and $\varepsilon_{Se}/k_B = 45.3$ K, where k_B is the Boltzmann constant. The Lorentz-Berthelot mixing rules (also known arithmetic mixing) were used for the LJ interactions between Pb and Se. The LJ term was truncated at a cutoff distance of 10 Å; the Coulomb term was calculated using a multilevel summation method (40). Calculations based on this potential have shown excellent agreements with the experimental and quantum mechanical results in regard to the lattice parameters and elastic constants. In addition, it has been used to reveal qualitatively correct pictures of particle shape changes during fusion at finite temperatures.

Nanocrystals with a strong electric dipole are generally considered the result of an uneven distribution of the polar {111} facets (10, 32), although a recent study showed that crystal symmetry breaking in the PbSe rock salt structure may also play a role (14). For nanocrystals with a stoichiometric (i.e., 4:4) distribution of Pb- and Se-terminated {111} facets, the <100> direction presents the highest dipole possibility and the largest dipole strength (33). We constructed a model of polar nanocrystals based on our experimentally determined result of the nanocrystal morphology (e.g., 20 layers along <100> direction) and a stoichiometric distribution of Pb- and Se-terminated {111} facets to produce the highest dipole strength. Dimer or trimer structures were built by aligning polar nanocrystals in a box with a 2-nm internanocrystal gap distance and a dipole direction along the internanocrystal vector. Then, MD simulations were run in a canonical assemble at 300 K in vacuum, with a time step of 1 fs for no less than 100 ps.

SUPPLEMENTARY MATERIALS

Supplementary material for this article is available at http://advances.sciencemag.org/cgi/content/full/5/6/eaaw5623/DC1

Electron beam effects during in situ TEM characterization

Internanocrystal interaction responsible for nanocrystal deformation
Kinetics of superlattice phase transitions in EG and EDA/EG
Perspective and open questions
Fig. S1. Schematic illustration of the liquid cell fabrication and real-time in situ TEM imaging of nanocrystal superlattice phase transitions.
Fig. S2. STEM images of randomly oriented nanocrystals in initial unconnected hexagonal superlattice.
Fig. S3. Moving-apart motion of neighboring nanocrystals during superlattice phase transitions.
Fig. S4. Reversible deformation of nanocrystals marked by 7 and 10.
Fig. S5. Retained deformation of nanocrystals during the oriented attachment in EDA solution.
Fig. S6. Reduced deformation of nanocrystals during the superlattice transformation in EG.
Fig. S7. Different pathways of superlattice transformations in EG and EDA/EG.
Fig. S8. EDS analyses of superlattices before and after phase transitions.
Fig. S9. Schematic of EDA-induced ligand removal.
Fig. S10. Molecular dynamics simulation on the deformability of nondipolar PbSe nanocrystals.
Movie S1. In situ liquid-phase TEM movie showing the phase transition of PbSe nanocrystals in EDA solution.
Movie S2. Reconstructed 3D atomistic model of PbSe nanocrystals in unconnected hexagonal superlattices.
Movie S3. In situ liquid-phase TEM movie showing the dynamic deformability of nanocrystals in EDA solution.
Movie S4. In situ liquid-phase TEM movie showing the reversible deformation of nanocrystals in EDA solution.
Movie S5. In situ liquid-phase TEM movie showing the transformation from a hexagonal superlattice to two nanocrystal chains in EDA solution.
Movie S6. In situ liquid-phase TEM movie showing retained deformation of nanocrystals during the oriented attachment in EDA solution.
Movie S7. In situ liquid-phase TEM movie showing the lattice alignment of neighboring nanocrystals during the oriented attachment in EDA solution.
Movie S8. In situ liquid-phase TEM movie showing the phase transition from hexagonal to square superlattices in pure EG.
Movie S9. In situ liquid-phase TEM movie showing reduced deformation of nanocrystals during the superlattice transformation in EG.
Movie S10. In situ heating TEM movie showing no perceptible deformation of individual nanocrystals without introducing any EDA or EG solution.

REFERENCES AND NOTES

1. J. A. Hollingsworth, V. I. Klimov, *Nanocrystal Quantum Dots* (CRC Press, 2010), pp. 1–62.
2. M. V. Kovalenko, L. Manna, A. Cabot, Z. Hens, D. V. Talapin, C. R. Kagan, V. I. Klimov, A. L. Rogach, P. Reiss, D. J. Milliron, P. Guyot-Sionnnest, G. Konstantatos, W. J. Parak, T. Hyeon, B. A. Korgel, C. B. Murray, W. Heiss, Prospects of nanoscience with nanocrystals. *ACS Nano* **9**, 1012–1057 (2015).
3. A. Banerjee, D. Bernoulli, H. Zhang, M.-F. Yuen, J. Liu, J. Dong, F. Ding, J. Lu, M. Dao, W. Zhang, Y. Lu, S. Suresh, Ultralarge elastic deformation of nanoscale diamond. *Science* **360**, 300–302 (2018).
4. J. Sun, L. He, Y.-C. Lo, T. Xu, H. Bi, L. Sun, Z. Zhang, S. X. Mao, J. Li, Liquid-like pseudoelasticity of sub-10-nm crystalline silver particles. *Nat. Mater.* **13**, 1007–1012 (2014).
5. F. F. Tao, M. Salmeron, In situ studies of chemistry and structure of materials in reactive environments. *Science* **331**, 171–174 (2011).
6. M. P. Boneschanscher, W. H. Evers, J. J. Geuchies, T. Altantzis, B. Goris, F. T. Rabouw, S. A. P. Van Rossum, H. S. J. van der Zant, L. D. A. Siebbeles, G. Van Tendeloo, I. Swart, J. Hilhorst, A. V. Petukhov, S. Bals, D. Vanmaekelbergh, Long-range orientation and atomic attachment of nanocrystals in 2D honeycomb superlattices. *Science* **344**, 1377–1380 (2014).
7. C. van Overbeek, J. L. Peters, S. A. P. van Rossum, M. Smits, M. A. van Huis, D. Vanmaekelbergh, Interfacial self-assembly and oriented attachment in the family of PbX (X = S, Se, Te) nanocrystals. *J. Phys. Chem. C* **122**, 12464–12473 (2018).
8. C. S. Sandeep, J. M. Azpiroz, W. H. Evers, S. C. Boehme, I. Moreels, S. Kinge, L. D. Siebbeles, I. Infante, A. J. Houtepen, Epitaxially connected PbSe quantum-dot films: Controlled neck formation and optoelectronic properties. *ACS Nano* **8**, 11499–11511 (2014).
9. K. Whitham, J. Yang, B. H. Savitzky, L. F. Kourkoutis, F. Wise, T. Hanrath, Charge transport and localization in atomically coherent quantum dot solids. *Nat. Mater.* **15**, 557–563 (2016).
10. K.-S. Cho, D. V. Talapin, W. Gaschler, C. B. Murray, Designing PbSe nanowires and nanorings through oriented attachment of nanoparticles. *J. Am. Chem. Soc.* **127**, 7140–7147 (2005).
11. C. Schliehe, B. H. Juarez, M. Pelletier, S. Jander, D. Greshnykh, M. Nagel, A. Meyer, S. Foerster, A. Kornowski, C. Klinke, H. Weller, Ultrathin PbS sheets by two-dimensional oriented attachment. *Science* **329**, 550–553 (2010).

12. W. H. Evers, J. M. Schins, M. Aerts, A. Kulkarni, P. Capiod, M. Berthe, B. Grandidier, C. Delerue, H. S. J. van der Zant, C. van Overbeek, J. L. Peters, D. Vanmaekelbergh, L. D. A. Siebbeles, High charge mobility in two-dimensional percolative networks of PbSe quantum dots connected by atomic bonds. *Nat. Commun.* **6**, 8195 (2015).

13. E. Sutter, P. Sutter, A. V. Tkachenko, R. Krahne, J. De Graaf, M. Arciniegas, L. Manna, In situ microscopy of the self-assembly of branched nanocrystals in solution. *Nat. Commun.* **7**, 11213 (2016).

14. F. Bertolotti, D. N. Dirin, M. Ibáñez, F. Krumeich, A. Cervellino, R. Frison, O. Voznyy, E. H. Sargent, M. V. Kovalenko, A. Guagliardi, N. Masciocchi, Crystal symmetry breaking and vacancies in colloidal lead chalcogenide quantum dots. *Nat. Mater.* **15**, 987–994 (2016).

15. C. A. S. Batista, R. G. Larson, N. A. Kotov, Nonadditivity of nanoparticle interactions. *Science* **350**, 1242477 (2015).

16. J. J. Geuchies, C. van Overbeek, W. H. Evers, B. Goris, A. . de Backer, A. P. Gantapara, F. T. Rabouw, J. Hilhorst, J. L. Peters, O. Konovalov, A. V. Petukhov, M. Dijkstra, L. D. A. Siebbeles, S. van Aert, S. Bals, D. Vanmaekelbergh, In situ study of the formation mechanism of two-dimensional superlattices from PbSe nanocrystals. *Nat. Mater.* **15**, 1248–1254 (2016).

17. M. C. Weidman, D.-M. Smilgies, W. A. Tisdale, Kinetics of the self-assembly of nanocrystal superlattices measured by real-time in situ x-ray scattering. *Nat. Mater.* **15**, 775–781 (2016).

18. M. Huang, C.-H. Hsu, J. Wang, S. Mei, X. Dong, Y. Li, M. Li, H. Liu, W. Zhang, T. Aida, W.-B. Zhang, K. Yue, S. Z. D. Cheng, Selective assemblies of giant tetrahedra via precisely controlled positional interactions. *Science* **348**, 424–428 (2015).

19. N. D. Loh, S. Sen, M. Bosman, S. F. Tan, J. Zhong, C. A. Nijhuis, P. Král, P. Matsudaira, U. Mirsaidov, Multistep nucleation of nanocrystals in aqueous solution. *Nat. Chem.* **9**, 77–82 (2017).

20. R. E. Schreiber, L. Houben, S. G. Wolf, G. Leitus, Z.-L. Lang, J. J. Carbo, J. M. Poblet, R. Neumann, Real-time molecular scale observation of crystal formation. *Nat. Chem.* **9**, 369–373 (2017).

21. H.-G. Liao, L. Cui, S. Whitelam, H. Zheng, Real-time imaging of Pt$_3$Fe nanorod growth in solution. *Science* **336**, 1011–1014 (2012).

22. D. Li, M. H. Nielsen, J. R. Lee, C. Frandsen, J. F. Banfield, J. J. De Yoreo, Direction-specific interactions control crystal growth by oriented attachment. *Science* **336**, 1014–1018 (2012).

23. J. M. Yuk, J. Park, P. Ercius, K. Kim, D. J. Hellebusch, M. F. Crommie, J. Y. Lee, A. Zettl, A. P. Alivisatos, High-resolution EM of colloidal nanocrystal growth using graphene liquid cells. *Science* **336**, 61–64 (2012).

24. H.-G. Liao, D. Zherebetskyy, H. Xin, C. Czarnik, P. Ercius, H. Elmlund, M. Pan, L.-W. Wang, H. Zheng, Facet development during platinum nanocube growth. *Science* **345**, 916–919 (2014).

25. F. M. Ross, Opportunities and challenges in liquid cell electron microscopy. *Science* **350**, aaa9886 (2015).

26. X. Ye, M. R. Jones, L. B. Frechette, Q. Chen, A. S. Powers, P. Ercius, G. Dunn, G. M. Rotskoff, S. C. Nguyen, V. P. Adiga, A. Zettl, E. Rabani, P. L. Geissler, A. P. Alivisatos, Single-particle mapping of nonequilibrium nanocrystal transformations. *Science* **354**, 874–877 (2016).

27. Y. Sun, X. Zuo, S. K. Sankaranarayanan, S. Peng, B. Narayanan, G. Kamath, Quantitative 3D evolution of colloidal nanoparticle oxidation in solution. *Science* **356**, 303–307 (2017).

28. W. F. McClune, *Powder Diffraction File Alphabetical Index Inorganic Phase* (JCPDS, 1980).

29. J. L. Peters, K. H. W. van den Bos, S. Van Aert, B. Goris, S. Bals, D. Vanmaekelbergh, Ligand-induced shape transformation of PbSe nanocrystals. *Chem. Mater.* **29**, 4122–4128 (2017).

30. P. Schapotschnikow, M. A. van Huis, H. W. Zandbergen, D. Vanmaekelbergh, T. J. Vlugt, Morphological transformations and fusion of PbSe nanocrystals studied using atomistic simulations. *Nano Lett.* **10**, 3966–3971 (2010).

31. W. H. Evers, B. Goris, S. Bals, M. Casavola, J. de Graaf, R. van Roij, M. Dijkstra, D. Vanmaekelbergh, Low-dimensional semiconductor superlattices formed by geometric control over nanocrystal attachment. *Nano Lett.* **13**, 2317–2323 (2012).

32. M. Klokkenburg, A. J. Houtepen, R. Koole, J. W. de Folter, B. H. Erne, E. van Faassen, D. Vanmaekelbergh, Dipolar structures in colloidal dispersions of PbSe and CdSe quantum dots. *Nano Lett.* **7**, 2931–2936 (2007).

33. K. Bian, J. J. Choi, A. Kaushik, P. Clancy, D.-M. Smilgies, T. Hanrath, Shape-anisotropy driven symmetry transformations in nanocrystal superlattice polymorphs. *ACS Nano* **5**, 2815–2823 (2011).

34. N. C. Anderson, M. P. Hendricks, J. J. Choi, J. S. Owen, Ligand exchange and the stoichiometry of metal chalcogenide nanocrystals: Spectroscopic observation of facile metal-carboxylate displacement and binding. *J. Am. Chem. Soc.* **135**, 18536–18548 (2013).

35. Z. Fan, L.-C. Lin, W. Buijs, T. J. Vlugt, M. A. Van Huis, Atomistic understanding of cation exchange in PbS nanocrystals using simulations with pseudoligands. *Nat. Commun.* **7**, 11503 (2016).

36. R. K. Mishra, R. J. Flatt, H. Heinz, Force field for tricalcium silicate and insight into nanoscale properties: Cleavage, initial hydration, and adsorption of organic molecules. *J. Phys. Chem. C* **117**, 10417–10432 (2013).

37. H. Heinz, H. Ramezani-Dakhel, Simulations of inorganic–bioorganic interfaces to discover new materials: Insights, comparisons to experiment, challenges, and opportunities. *Chem. Soc. Rev.* **45**, 412–448 (2016).

38. X. Peng, A. Abelson, Y. Wang, C. Qian, J. Shangguan, Q. Zhang, L. Yu, Z.-W. Yin, W. Zheng, K. C. Bustillo, X. Guo, H.-G. Liao, S.-G. Sun, M. Law, H. Zheng, In situ TEM study of the degradation of PbSe nanocrystals in air. *Chem. Mater.* **31**, 190–199 (2018).

39. S. Plimpton, Fast parallel algorithms for short-range molecular dynamics. *J. Comput. Phys.* **117**, 1–19 (1995).

40. D. J. Hardy, J. E. Stone, K. Schulten, Multilevel summation of electrostatic potentials using graphics processing units. *Parallel Comput.* **35**, 164–177 (2009).

Science Advances

Dynamic deformability of individual PbSe nanocrystals during superlattice phase transitions

Yu Wang, Xinxing Peng, Alex Abelson, Penghao Xiao, Caroline Qian, Lei Yu, Colin Ophus, Peter Ercius, Lin-Wang Wang, Matt Law and Haimei Zheng

ARTICLE TOOLS	http://advances.sciencemag.org/content/5/6/eaaw5623
SUPPLEMENTARY MATERIALS	http://advances.sciencemag.org/content/suppl/2019/06/03/5.6.eaaw5623.DC1
REFERENCES	This article cites 38 articles, 13 of which you can access for free http://advances.sciencemag.org/content/5/6/eaaw5623#BIBL
PERMISSIONS	http://www.sciencemag.org/help/reprints-and-permissions

Use of this article is subject to the Terms of Service